Report on Tevatron Modeling and Accelerator Physics

Version 1

June 13, 2003

Contents

1 Introduction

The Tevatron Upgrade project is based primarily on increasing the number of antiprotons available for collisions in the Tevatron per store, and the ability to produce and store antiprotons at an increased rate. While this implies improvements to the Antiproton Source, the Recycler Ring in its role as an antiproton storage ring with electron cooling, as well as to improvements to the Proton Source and Main Injector operations, the Tevatron collider must be able to accept the increased beam intensity and perform appropriate manipulations to bring these more intense beams into collision. The purpose of this text is to bring together a collection of topics documenting the current understanding of the Tevatron and its present and future operation within the context of the upgrade plan.

We begin by discussing recent developments in the understanding of the Tevatron's optical properties. Identification of error sources and subsequent understanding of corrector settings have led to detailed models of the synchrotron which reproduce measured beam trajectories to roughly the accuracy of the Beam Position Monitor system. Understanding at this level is important to have in order to flush out more subtle effects such as those from beam-beam interactions.

Next, we look at our understanding of the development of luminosity throughout a collider store, with emphasis on beam-gas interactions and diffusive effects. A model is presented which describes our current understanding of the present operation and this model is used to estimate the gains from increased luminosity due to higher antiproton stacks using the Recycler Ring with electron cooling.

The mutual interactions of the proton and antiproton beams at 72 locations about the circumference as they circulate the Tevatron play a critical role in the development of the stable phase space region, especially for the antiproton beam. A major section explores our understanding of the Tevatron beam-beam interactions including experimental results and theoretical studies which help lead toward optimization of tunes, helical orbits, and nonlinear corrections.

With the increased beam intensities foreseen in the upgrade plan, beam instabilities become more of an issue. Already being dealt with at present Run II bunch intensities, the current understanding of the observed Strong Head-Tail instability in the Tevatron as well as the "dancing bunch" phenomenon observed primarily wih uncoalesced bunches are described. With these studies come a more detailed understanding of the Tevatron impedance, as well as improved diagnostic equipment and software for studying these effects.

Finally, further mitigation of beam-beam interactions is discussed in the last two sections. One section is devoted to recent investigations into better optimization of the electrostatic separators to provide a more robust separation scheme. Improvements using the system "as is" with additional polarity reversal switches (being implemented) as well as the use of stronger separators are discussed. The last section is devoted to the topic of beam-beam

compensation using electron beams (Tevatron Electron Lens), and through the possible use of wires to generate compensating long-range interactions with the antiproton bunches as first proposed for the LHC.

2 Present Picture of Tevatron Configuration

Throughout the start-up of Run II, several issues have surfaced which were not present, or not seen as detrimental, during Run I. These include the repeated deterioration of the closed orbit requiring orbit smoothing every two weeks or so, the inability to correct the closed orbit to desired positions due to various correctors running at maximum limits, regions of systematically strong vertical dipole corrections, the drifting of tunes and transverse coupling during 150 GeV injection operations akin to the well-known drifting of chromaticity at this energy, and the identification of very strong coupling of the transverse degrees-of-freedom. Many of these effects have been dealt with operationally, leading to tune drift compensation and coupling drift compensation software for running correction magnet circuits automatically during injection dwell times, for example. However, much effort also has gone into understanding the sources of errors responsible for these effects, a synopsis of which is presented in the following subsections.

2.1 Strong Systematic Steering Correction

Regions of the Tevatron contain vertical steering magnets whose average strength is required to be non-zero in order to produce a smooth trajectory as seen on the Beam Position Monitors. Compared to the 0.7 μrad average horizontal steering corrector strength, the vertical correctors have a ring-wide average of about 16 μrad, and areas of the Tevatron have average strengths of 70-90 μrad averaged over distances of 400 m or so. At 1 TeV, the maximum strength of a corrector is a little more than 100 μrad and so the available correction for general beam steering is limited in these locations. The interpretation of this effect is that these areas contain magnets which are systematically rolled toward the inside of the tunnel. This was verified by magnet roll angle measurements performed in October 2002, and January 2003.

As depicted in Figure 1, the systematic corrections produce a "scalloped" vertical trajectory through the bending regions.[1] Though the BPM system might read zero displacements, the beam will actually undergo $\sim$0.5 mm excursions through these regions, assuming the magnets are rolled about the beampipe axis. In reality, the magnets may actually be rolled about an axis near the base of the magnet stand or perhaps near the floor implying that the scalloped beam trajectory would be displaced ever further from the center of the magnet coil. (The tunnel measurements only revealed the roll angles. A full magnet survey is required to establish the spatial placement of the magnet with respect to the particle tra-

jectory.) Figure 2 shows the correlation between measured roll angles and vertical corrector settings.

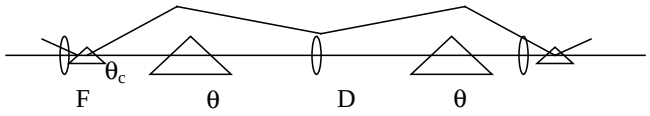

Figure 1: **Correction of vertical trajectory generated by rolled dipole magnets in a FODO cell.**

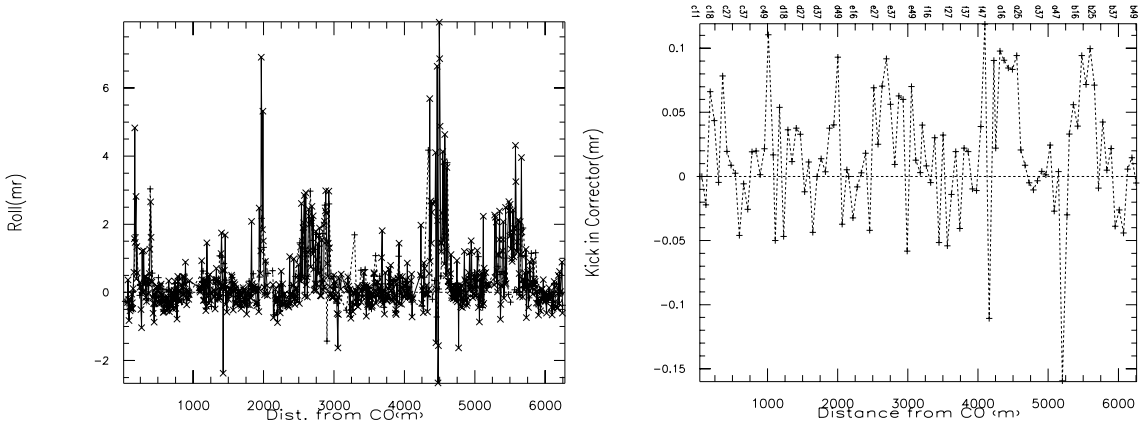

Figure 2: **Roll measurements and vertical dipole corrector settings, in mrad.**

Since the Tevatron dipoles have a strong sextupole component, a systematic vertical offset will feed-down into a coupling term between the horizontal and vertical motion. The sextupole component is also known to vary logarithmically with time due to persistent current effects at low field, hence the coupling would vary with time accordingly. It is thought that this effect explains much of the observed tune drift behavior during the Tevatron injection process, though it is not nearly enough to explain the large skew quadrupole corrector settings.

Although not directly related to magnet rolls, the tunes are observed to drift logarithmically with time at injection as well. A study was performed which showed that the average radial position of the centers of the chromaticity adjustment sextupoles near focusing quadrupole magnets is different than the average radial center of the chromaticity sextupole near defocusing quadrupoles.[2] These sextupoles' power supplies are programmed to vary logarithmically with time to keep the chromaticity steady as the persistent current sextupole moment of the main dipole magnets changes at injection. Thus, an average radial offset in one or both of the correction circuits will generate a feed-down tune shift, helping to explain the observed effect. It is thought that this misalignment may not be the entire story, but certainly plays a part and adds to the operational confusion.

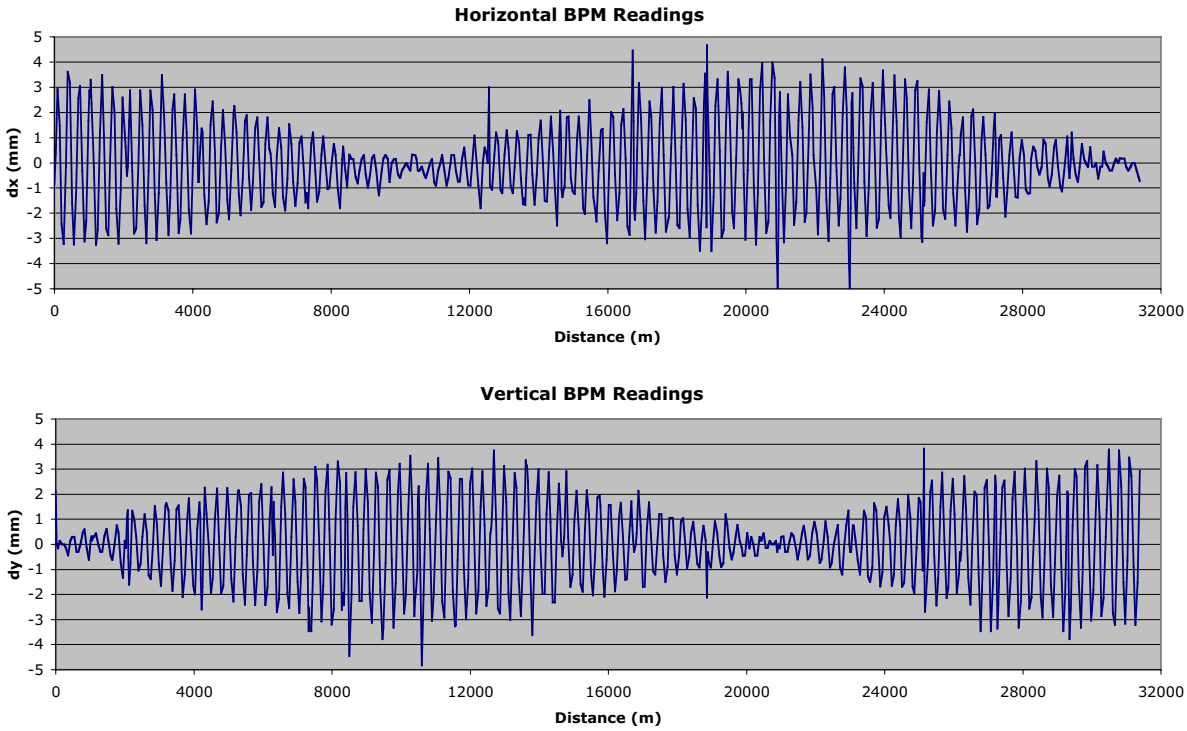

Figure 3: Data taken in February, 2003, showing horizontal motion coupling fully into the vertical plane in less than 2 turns. One revolution about the Tevatron is about 6283 m; the data are for 5 consecutive turns.

2.2 Strong Systematic Transverse Coupling

The transverse coupling generated by orbit feed-down through rolled dipole magnets and the estimated coupling due to observed quadrupole rolls do not account for the strong correction required of the main skew quad circuit. Taken together, these effects are strong enough to explain a correction of the minimum difference between the two transverse tunes of amount $\Delta\nu \approx 0.03$. However, the setting required of the main skew quadrupole correction circuit to decouple the Tevatron is indicative of a minimum tune difference an order of magnitude larger. An experiment was performed[3] in which protons were injected into the Tevatron with all skew quadrupole correctors turned off. The result, given in Figure 3, shows pure horizontal motion being coupled completely into the vertical plane within about 1.5 revolutions. The fact that the coupling builds up gradually and not at a a few localized sources is indicative of a uniformly distributed source of skew quadrupole fields. The 3-turn period of the coupling is consistent with a tune split of order 0.3. It was quickly noted that a systematic skew quadrupole term, $a_1 \equiv \partial(B_x/\partial x)/B_0$, would account for this behavior, and would need to be of order

$$2Fa_1 = 0.3 \quad \rightarrow \quad a_1 = 1.5 \times 10^{-4}\text{inch}^{-1},$$

or 1.5 "units," where $F = 25.4$ m is the focal length of a standard arc quadrupole.

Almost simultaneously, dipole magnets in the Tevatron tunnel had been examined to see if the cold masses could have rotated inside their cryostats. Instead, what was found was that in almost every instance (about 80 magnets have been measured) the magnet coil has dropped systematically by roughly 4 mils throughout the accelerator, presumably caused by a compression of G-11 spacers used in the cold mass assembly. An off-centered coil within the iron yoke leads to a skew quadrupole moment, and a 4 mil displacement leads directly to a value for a_1 of 1.0 - 1.5 units.[4] A plan is being developed to see if it is feasible to re-shim magnets in the tunnel.

Even though the "global" coupling (minimum tune split) can be compensated easily with the skew quadrupole circuits already in place in the Tevatron, the "local" coupling is strong enough to have effects on the understanding of damper systems, emittance measurement interpretation, injection mismatches, and so forth. For example, a larger-than-normal vertical dispersion is seen in the Tevatron, and is easily attributed to the uniformly distributed a_1 source, and its lumped "correction."[5] It also changes by large amounts depending upon which skew quadrupole circuits are adjusted to reduce the tune split. For reference, a mismatch of the Tevatron and Main Injector dispersion functions by 1 m can lead to an emittance growth of 5π mm-mrad during transfer of coalesced (large momentum spread) bunches.

2.3 Helical Orbits

The sensitivity of magnet misalignments and associated tune, chromaticity, and coupling control is exacerbated by the fact that proton and antiproton beams circulate the Tevatron on separate, helical orbits during a store. The situation is worse at the injection energy where the beams are larger, requiring larger separation in the face of field nonlinearities which are more prominent at lower magnet excitation. The betatron tunes and transverse coupling (global, again) are independently controlled on these orbits by using so-called "feed-down" sextupoles and skew sextupoles where the settings depend upon the trajectories through these devices. Additionally, orbit offsets and fluctuations of lattice functions (amplitude functions, dispersion functions, and phase advances) due to magnet imperfections and misalignments make tuning the synchrotron not only harder, but less reproducible. This view was supported when two record-breaking weeks of integrated luminosity followed an extensive orbit-smoothing exercise in late April 2003.

Much more discussion of helical orbits is found in a later section. Here, it suffices to note that much can be done to improve today's situation. The present helical orbit operation is limited by the continued use of 2 electrostatic separators at injection, and an inadequate transformation of the helical orbits throughout the low-beta squeeze just prior to collisions. New work has been done on this issue and is one of the topics of discussion later in Section 5. It should be pointed out, however, that once a new separator scheme is chosen the feed-down circuits used for fine tuning the transverse tunes, chromaticity, and coupling will need to be re-optimized. This is possible due to the flexibility of individual magnets and power supplies used for this purpose.

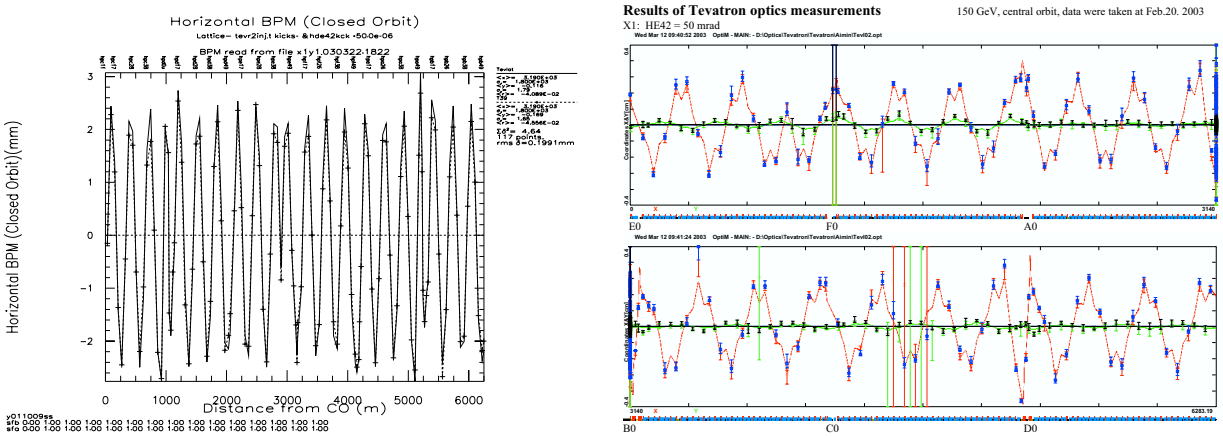

Figure 4: Comparison of Beam Position Monitor data with results from modeling calculations using two codes, TEVLAT (left) and OptiM (right). The data correspond to the response of the beam to a single-turn transverse deflection in the horizontal plane.

2.4 General Remarks

Much of the above understanding of corrector settings, magnet misalignments, and the effects of strong coupling has been obtained during the past eight months, enabling the development of improved, more detailed models of the Tevatron. Low-order optics calculations using a variety of programs can now readily explain observed orbit distortions, coupling effects, and corrector strengths.[6] (See Figure 4.) It is clear that not all magnetic error fields in the installed Tevatron can easily be known. The magnetic measurements performed over 20 years ago were done without knowledge of persistent current effects, and without foreseeing mechanical motion within magnet components. Additionally, the magnet correction systems were not designed to deal with today's problems. For example, the steering correctors were placed to adjust for the errors and misalignments of its neighboring 8 dipole magnets and 2 quadrupole magnets. To work properly, this system assumes a smooth source of errors – large point source excursions were assumed to be fixed by re-alignment in the tunnel. Likewise, the skew quadrupole correctors adjust for errors in the neighboring 16 dipole magnets and 4 quadruole magnets. However, local skew quadrupole correctors were removed in the vicinity of the collider detectors to make room for low-beta optics quadrupoles. Variations in vertical dispersion due to the skew correctors was not considered in the original circuit design as this was not an issue for slow resonant extraction, and was likewise not considered during the redesign of the low-beta insertion optics. On the other hand, the present knowledge of two major effects – systematic a_1 and magnet alignment in the tunnel – present a straightforward path for improvement in Tevatron operations. Progress toward higher-luminosity operation will likely require better alignment and a better controlled configuration of Tevatron components and will most likely also require re-shimming of dipole magnets in the tunnel to correct the large systematic skew quadrupole moment. These tasks are specifically included in the Luminosity Upgrade Program.

References

[1] M. Syphers, "Strong Systematic Steering Correction in Regions of the Tevatron," Beams-doc-491, March 2003.

[2] M. Martens, "Measurement of the Tevatron tune shift versus RF frequency and strength of the T:SF and T:SD circuits," Beams-doc-436, February 2003.

[3] D. Edwards and M. Syphers, "Strong Transverse Coupling in the Tevatron," EXP-203, Beams-doc-501, March 2003.

[4] A. V. Tollestrup, "The Amateur Magnet Builder's Handbook," Fermilab note UPC No. 86, February 1979; and M. Syphers, "Estimate of Skew Quadrupole Field in Tevatron Dipoles due to Creep," Beams-doc-513, March 2003.

[5] M. Syphers, "Skew Quadrupole Tuning and Vertical Dispersion in the Tevatron," Beams-doc-611, June 2003.

[6] Significant modeling has been performed using TEVLAT (N. Gelfand, "Dispersion and Orbit Distortions in the Tevatron: A Comparison of Measurements with a Computer Model," Fermilab TM-2211, May 2003), OPTIM (V. Lebedev, private communication), and MAD (M. Xiao, B. Erdelyi, T. Sen, "Tevatron Beam-Beam Simulations at Injection Energy," submitted PAC 2003 conf. proc.).

3. Basic Mechanisms of Beam Diffusion and Luminosity Lifetime

Numerous factors affect the Tevatron collider luminosity and its evolution in time. Each store is different and because of finite instrumentation accuracy it is practically impossible to state what was different or what came wrong for every particular store. Nevertheless the luminosity development is very similar for most of the stores. It is driven by some basic processes, which are not very sensitive to the details of distribution functions, and therefore the luminosity evolution can be described by comparatively simple parametric model developed in the following sections. The model takes into account the major beam heating and particle loss mechanisms. They are (1) the emittance growth and the particle loss due to scattering on the residual gas, (2) the particle loss and the emittance growth due to scattering in IPs, (3) the transverse and longitudinal emittance growth due to intrabeam scattering, (4) the bunch lengthening due to RF noise, and (5) the particle loss from the bucket due to heating of longitudinal degree of freedom. If the collider tunes are correctly chosen, the beam intensity is not too high, and the beams are well formed, then the beam-beam effects are not very important and the model describes the observed dynamics of beam parameters and the luminosity comparatively well. The developed model is applied to the luminosity evolution for the final Run II parameters at the end of this section. Detailed discussion of how the beam-beam effects and lattice non-linearities interact with diffusion and how they can be incorporated into the model postponed to Section 4.

3.1. Particle scattering and absorption on the residual gas and in IP

If aperture limitations are sufficiently large in comparison with the beam size ($A_{x,y} \geq 5\sigma_{x,y}$), then the multiple and single scattering on the residual gas atoms can be considered separately. In this case the single scattering causes the particle loss, while the multiple scattering causes the emittance growth.

The beam lifetime due to single scattering is described by the well-known formula

$$\tau_{scat}^{-1} == \frac{2\pi c r_p^{\,2}}{\gamma^2 \beta^3}\left(\sum_i Z_i (Z_i + 1)\left(\frac{\overline{\beta_x n_i}}{\varepsilon_{mx}} + \frac{\overline{\beta_y n_i}}{\varepsilon_{my}}\right)\right) + \sum_i n_i \sigma_i c\beta \quad , \qquad (1)$$

where $\overline{\beta_{x,y} n_i} = \int \beta_{x,y} n_i ds \Big/ C$ are the average gas density weighted by beta-functions, $\varepsilon_{mx,my}$ are the horizontal and vertical acceptances, r_p is the proton classical radius, γ and β are the relativistic factors, the summing is performed over all residual gas species, and the averaging is performed over ring circumference. The first addend is related to the electromagnetic scattering and the second one to the strong interaction. Taking into account that the scattering angle due to strong interactions ($\theta \sim m_\pi/\mathrm{p} \approx 140$ μrad) significantly exceeds rms angles in the beam (~7 μrad) σ_i can be considered to be the total nuclear cross section with sufficiently good accuracy. The beam based measurements of the average residual gas pressure yield that the average pressure in the ring is about 10^{-9} Torr of molecular nitrogen equivalent.[1] It is also verified by the results of the luminosity parametric model presented below. At the collision energy of 980 GeV the beam lifetime is dominated by the strong interaction.

The emittance growth rate due to multiple scattering is closely related to the electromagnetic part of the single scattering lifetime and is determined by the following formula[1]

$$\frac{d\varepsilon_{x,y}}{dt} = \frac{2\pi c r_p^{\,2}}{\gamma^2 \beta^3}\left(\sum_i \overline{\beta_{x,y} n_i} Z_i (Z_i + 1) L_c\right) \quad , \tag{2}$$

where L_c is the Coulomb logarithm ($L_c \approx 9$). Tables 1 and 2 present parameters used in the simulations. As far as we can judge now these parameters represent present vacuum conditions in Tevatron and we do not expect significant vacuum improvements in the future.

Table 1. Gas composition used in the simulations

Gas	H_2	CO	N_2	C_2H_2	CH_4	CO_2	Ar
Pressure [nTorr]	1.05	0.18	0.09	0.075	0.015	0.09	0.15

Table 2. Model parameters used in the simulations

Effective N_2 equivalent pressure, $\sum Z_i (Z_i + 1) n_i / (2 \cdot 7 \cdot 8)$	$1.04 \cdot 10^{-9}$ Torr
Average ring beta-functions, β_x/β_y	71.5 m/71.7 m
Normalized acceptance	720 mm mrad
Electromagnetic scattering lifetime	6000 hour
Nuclear scattering/absorption lifetime	405 hour
Total single scattering lifetime	380 hour
Normalized 95% emittance growth rate, $6\gamma d\varepsilon_{x,y}/dt$	0.194 mm mrad/hour

Similar to the gas scattering the scattering in the interaction point (IP) can be separated into the single scattering due to strong interaction and the emittance growth due to electromagnetic scattering. The total $\bar{p}p$ cross section consists of two parts: the inelastic cross section of 60 mbarn and the elastic cross section of 15 mbarn at 1 TeV energy. All particles scattered inelastically are lost immediately, while as shown in Ref.[2] about 40% of elastically scattered particles remain in the beam (within 3σ). That happens because the beta-functions in the IP are small and, consequently, particle angles are large; so that the scattering angles are comparable to the particle angles (~100 μrad). Summing effects of elastic and inelastic interactions we obtain the total cross section of particle loss equal to 69 mbarn.

The emittance growth due to electromagnetic scattering equal to

$$\frac{d\varepsilon_{x,y}}{dt} = \frac{4 r_p^{\,2} N L_{bb} f_0}{\gamma^2 \beta^3 \sqrt{(\varepsilon_{px} + \varepsilon_{py})(\varepsilon_{ax} + \varepsilon_{ay})}} \tag{3}$$

for one IP. Here ε_{px}, ε_{py}, ε_{ax} and ε_{ay} are the emittances for proton and antiproton beams, f_0 is the revolution frequency, L_{bb} is the Coulomb logarithm ($L_{bb} \approx 20$), and N is the number of particles in the counter-rotating bunch. For two IPs and present Tevatron parameters it yields the antiproton emittance growth rate of about 0.01 mm mrad/hour. Although

[1] We use the non-normalized rms emittances, ε_x, ε_y, in all formulas throughout this document; but all numerical values are quoted for the standard Fermilab emittance definition - the 95% normalized emittances, ε_{nx}, ε_{ny},. Two definitions are bound up by the following formula $\varepsilon_{nx,ny} = 6\gamma\, \varepsilon_{x,y}$.

emittance growth rate is almost negligible in comparison with gas scattering the nuclear absorption in the IP is the main mechanism for antiproton loss during collisions.

3.2. Intrabeam scattering

Another important diffusion mechanism is determined by intrabeam scattering (IBS). For the Tevatron collider parameters the longitudinal energy spread in the beam frame is significantly smaller than the transverse ones ($v_{||}/v_{\perp} \approx 0.02$ at collision energy, and $v_{||}/v_{\perp} \approx 0.15$ at injection energy). In this case comparatively simple IBS formulas can be used. Following reference [3] we can write the following expressions for the longitudinal and transverse emittance growth rates[2]

$$\frac{d\left(\sigma_{\Delta p/p}{}^2\right)}{dt} = \frac{r_p{}^2 cN}{4\sqrt{2}\gamma^3\beta^3\sigma_s}\left\langle \frac{\Xi_{||}\left(\theta_x,\theta_y\right)}{\sqrt{\theta_x{}^2+\theta_y{}^2}}\frac{L_C}{\sigma_x\sigma_y}\right\rangle_s , \tag{4}$$

$$\frac{d\varepsilon_{x,y}}{dt} = \frac{r_p{}^2 cN}{8\sqrt{2}\gamma^3\beta^3\sigma_s}\left\langle \frac{L_C}{\sigma_x\sigma_y\sqrt{\theta_x{}^2+\theta_y{}^2}}\begin{bmatrix} 2A_x\Xi_{||}\left(\theta_x,\theta_y\right)-\dfrac{\beta_x}{\gamma^2}\Xi_{\perp}\left(\theta_x,\theta_y\right) \\ -\dfrac{\beta_y}{\gamma^2}\Xi_{\perp}\left(\theta_y,\theta_x\right)\end{bmatrix}\right\rangle_s . \tag{5}$$

Here $\sigma_{\Delta p/p} \equiv \sqrt{\left(p_{||}/p\right)^2}$ is the rms momentum spread, σ_s is the rms bunch length,

$$\sigma_x = \sqrt{\varepsilon_x\beta_y + D_x{}^2\theta_{||}{}^2}\,, \qquad \sigma_y = \sqrt{\varepsilon_y\beta_y}\,,$$
$$\theta_x = \sqrt{\frac{\varepsilon_x}{\beta_x}\left(1+\frac{\left(D_x'\beta_x+\alpha_x D_x\right)^2\sigma_{\Delta p/p}{}^2}{\varepsilon_x\beta_x+D_x{}^2\sigma_{\Delta p/p}{}^2}\right)}\,, \qquad \theta_y = \sqrt{\varepsilon_y/\beta_y} \tag{6}$$

are the rms sizes and the local angular spreads along the ring, β_x, β_y, α_x and α_y, are beta- and alpha-functions, D_x and D_x' are the dispersion and its derivative, $\langle\ \rangle_s$ denotes averaging over the ring,

$$A_x = \frac{D_x{}^2+\left(D_x'\beta_x+\alpha_x D_x\right)^2}{\beta_x} \tag{7}$$

is the horizontal motion invariant, and

$$L_C = \ln\left(\frac{r_{\max}}{r_{\min}}\right), \quad r_{\max} = \min\left(\sigma_x,\sigma_y,\sqrt{\frac{\theta_x{}^2+\theta_y{}^2}{Nr_p}\gamma^3\beta^2\sigma_x\sigma_y\sigma_s}\right), \quad r_{\min} = \frac{2r_p}{\gamma^2\beta^2\left(\theta_x{}^2+\theta_y{}^2\right)} \tag{8}$$

is the Coulomb logarithm ($L_C \approx 23$). Functions

$$\Xi_{||}\left(x,y\right) \approx 1+\frac{\sqrt{2}}{\pi}\ln\left(\frac{x^2+y^2}{2xy}\right)-0.055\left(\frac{x^2-y^2}{x^2+y^2}\right)^2, \tag{9}$$

[2] A comparison of these equations with the Bjorken-Mtingwa formulas[4] for the case $v_{||} \ll v_{\perp}$ exhibited their identity when exact integral presentations are used for functions $\Xi_{||}(x,y)$ and $\Xi_{\perp}(x,y)$. In the case of their approximate representation considered here the results coincide within a few percent.

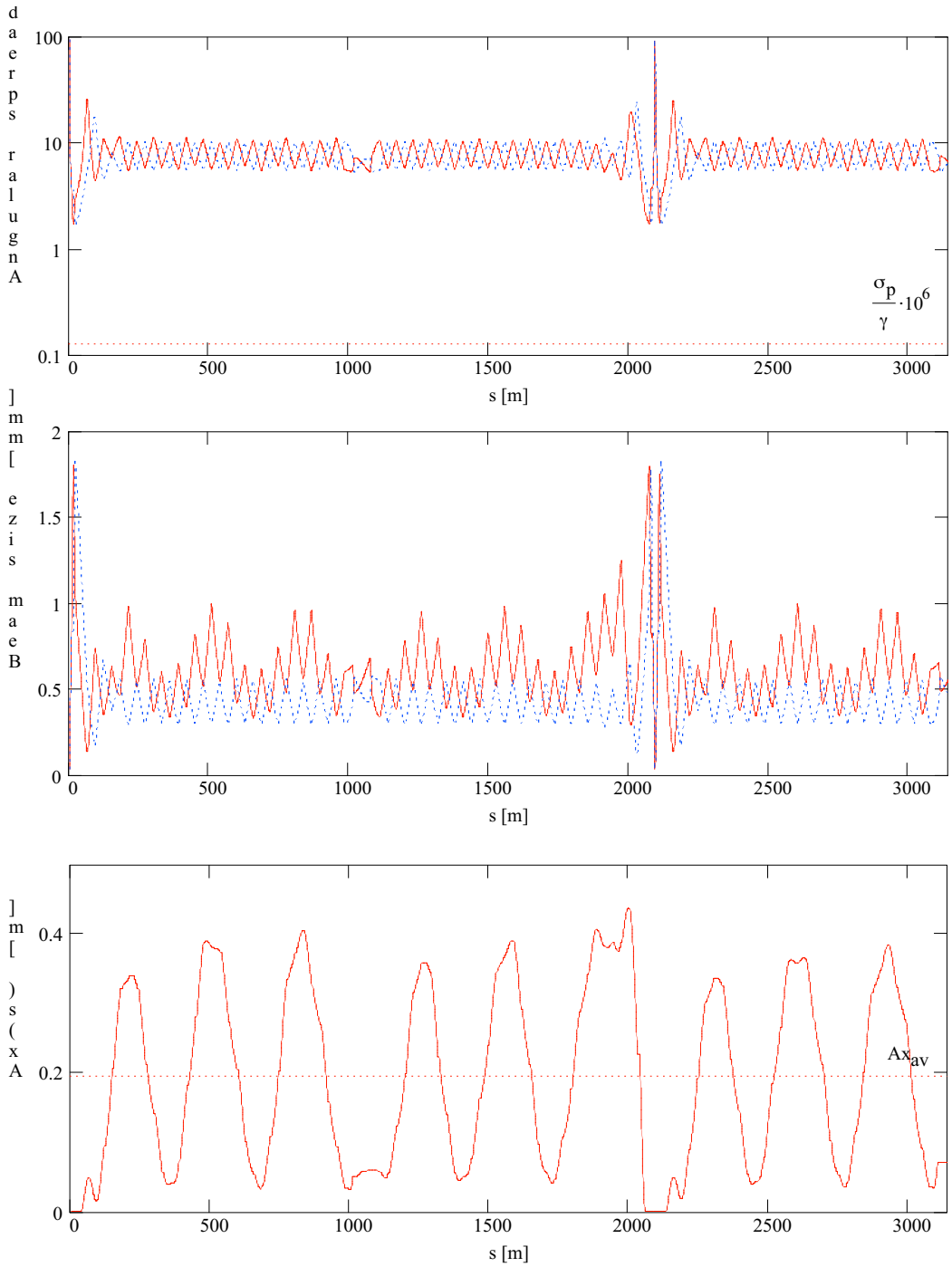

Figure 1. Rms angular spreads (top), rms beam sizes (center) and the horizontal motion invariant A_x (bottom) and for half Tevatron circumference (from B0 to E0); solid lines – horizontal degree of freedom, dashed lines – vertical degree of freedom. Transverse normalized 95% beam emittances are 19 mm mrad, longitudinal energy spread is $1.35 \cdot 10^{-4}$. Horizontal line on the top plot shows longitudinal "angle" in the beam frame.

$$\Xi_{\perp}(x,y) \approx 1 + \frac{2\sqrt{2}}{\pi}\ln\left(\frac{\sqrt{3x^2+y^2}}{2y^2}x\right) + \frac{0.5429\ln(y/x)}{\sqrt{1+\ln^2(y/x)}} \qquad (10)$$

approximate exact results (obtained for Gaussian distribution for all three degrees of freedom) with accuracy better than a few percent. That is sufficiently good for all practical applications. The energy conservation requires $\Xi_{\perp}(x,y) + \Xi_{\perp}(y,x) = 2\Xi_{\parallel}(x,y)$, which is fulfilled with better than 1% accuracy.

Tevatron has sufficiently smooth lattice and therefore IBS can be described with good accuracy in the smooth approximation. In this case Eq. (4) and (5) can be rewritten as following

$$\begin{bmatrix} d\sigma_{\Delta p/p}{}^2/dt \\ d\varepsilon_x/dt \\ d\varepsilon_y/dt \end{bmatrix} = \frac{r_p{}^2 c N L_C \Xi_{\parallel}(\bar{\theta}_x, \bar{\theta}_y)}{4\sqrt{2}\gamma^3\beta^3\bar{\sigma}_x\bar{\sigma}_y\sigma_s\sqrt{\bar{\theta}_x{}^2+\bar{\theta}_y{}^2}} \begin{bmatrix} 1 \\ \bar{A}_x(1-\kappa) \\ \bar{A}_x\kappa \end{bmatrix} \quad , \qquad (11)$$

where

$$\bar{\sigma}_x = \sqrt{\varepsilon_x\bar{\beta}_y + \bar{D}_x{}^2\sigma_{\Delta p/p}{}^2}\,, \qquad \bar{\sigma}_y = \sqrt{\varepsilon_y\bar{\beta}_y}\,,$$
$$\bar{\theta}_x = \sqrt{\varepsilon_x/\bar{\beta}_x}\,, \qquad \bar{\theta}_y = \sqrt{\varepsilon_y/\bar{\beta}_y}\,. \qquad (12)$$

For Tevatron the averaged beta-functions, the dispersion and the horizontal motion invariant are $\bar{\beta}_x = R/\nu_x = 49$ m, $\bar{\beta}_y = R/\nu_y = 49$ m, $\bar{D}_x = \int D_x ds/2\pi R = 2.84$ m, and $\bar{A}_x = \int A_x ds/2\pi R = 0.2$ m. To get Eq. (11) we neglected in Eq. (5) the addends with $\Xi_{\perp}(x,y)$ which make only small correction but we introduced the coupling parameter κ which takes into account the redistribution of heating between horizontal and vertical degrees of freedom. Presently we do not know our optics with sufficient accuracy to calculate κ independently. An experimental value is about 0.4 is very large and seemingly is related to the strong coupling due to beam-beam effects.

Figure 1 presents beam sizes and angular spreads for half Tevatron at collisions. One can see that the longitudinal velocity spread is much smaller than the transverse one through the entire ring. That validates the use of simplified IBS formulas of Eqs. (4) and (5). Averaging these equations over the ring for beam parameters of Figure 1, the rms bunch length of 62 cm, zero coupling (κ = 0) and $1.6\cdot10^{11}$ protons/bunch yields the horizontal and longitudinal emittance growth lifetimes of 22.5 and 28.5 hours, correspondingly. The use of smooth approximation formulas of Eq. (11) yields 18.9 and 26.9 hours. As one can see the difference is sufficiently small and therefore the smooth approximation has been used in the described below parametric model.

3.3. Intensity loss and bunch lengthening due to diffusion

The length of the bunch in Tevatron is large and therefore a longitudinal diffusion causes particle loss from the bucket. The diffusion equation in a sinusoidal longitudinal potential can be written in the following form

$$\frac{\partial f}{\partial t} = \frac{\partial}{\partial I}\left(I\,\frac{D(I)}{dE/dI}\,\frac{\partial f}{\partial I}\right) \quad , \qquad (13)$$

where the action and the energy are

$$I = \frac{1}{2\pi}\oint p d\phi \quad , \quad E = \frac{p^2}{2} + \Omega_s{}^2(1-\cos\phi) \quad . \tag{14}$$

The solution of Eq. (13) was performed numerically for the case of constant diffusion, and zero initial length bunch, $f(I) = \delta(I)$. The boundary condition $f(I) = 0$ at the RF bucket boundary is used. It is justified by the fact that only small fraction (36/1113) of the buckets are filled. Particles, which leave the bucket, become smoothly distributed through the entire ring. That immediately drops particle density by almost 2 orders of magnitude. Additionally, particles are decelerated by synchrotron radiation and leave the ring in about 20 minutes after they left the bucket.

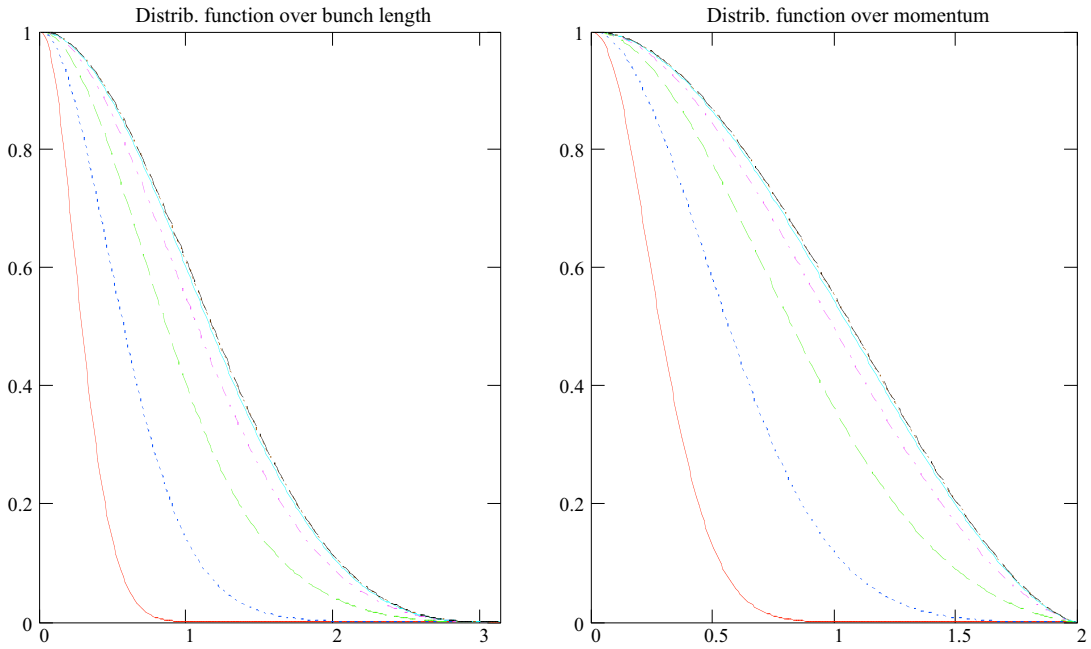

Figure 2. Dependence of distribution functions over bunch length and momentum on time obtained by numerical solving Eq. (13) for constant diffusion. Curves show the distribution sequentially for the following dimensionless times: $D\,t$ = 0.0625, 0.25, 0.562, 1.0, 1.56, 2.25, 3.06.

Resulting distribution functions over bunch length and momentum are presented in Figure 2. Figure 3 presents time dependence of rms bunch length and momentum on time, and Figure 4 presents relative bunch intensity on time. As one can see, initially, while the whole bunch is located in the linear part of potential well the rms bunch length and the momentum spread are equal and grow proportionally to $\sqrt{Dt}$. Then, when the potential well shallows, the bunch length grows faster than the momentum spread and, finally, both of them come to their asymptotic values: $\sigma_\phi \approx 0.930$ rad and $\sigma_p \approx 0.765$. At that time the intensity dependence on time and distribution functions also come to its asymptotic behaviors. The intensity decays exponentially, $I \propto \exp(-1.35Dt)$. As one can see from Figure 2 the asymptotic distribution function over bunch length is sufficiently close to the Gaussian, but the asymptotic distribution function over momentum is almost parabolic.

The results of simulations yield the following approximate relationships between the bunch parameters

$$\sigma_s \approx \Gamma_s \sigma_{\Delta p/p}\left(1+\frac{1}{4}\left(\frac{2\sigma_{\Delta p/p}}{\Delta P/P\big|_{sep}}\right)^2+\frac{1}{6}\left(\frac{2\sigma_{\Delta p/p}}{\Delta P/P\big|_{sep}}\right)^3\right) \quad , \tag{15}$$

$$\frac{1}{N}\frac{dN}{dt}\bigg|_L \approx \frac{2.425\,(2\pi\sigma_s)^7}{\lambda_{RF}{}^7+1.65\,(2\pi\sigma_s)^7}\left(\left(\frac{2\pi\Gamma_s}{\lambda_{RF}}\right)^2\frac{d\left(\sigma_{\Delta p/p}{}^2\right)}{dt}\bigg|_{IBS}+\frac{d\left(\sigma_\phi{}^2\right)}{dt}\bigg|_{RF}\right) \quad , \tag{16}$$

$$\frac{d\left(\sigma_{\Delta p/p}{}^2\right)}{dt}\bigg|_{total} \approx \left(1-\left(\frac{2\sigma_{\Delta p/p}}{0.765\Delta P/P\big|_{sep}}\right)^5\right)\left(\frac{d\left(\sigma_{\Delta p/p}{}^2\right)}{dt}\bigg|_{IBS}+\left(\frac{\lambda_{RF}}{2\pi\Gamma_s}\right)^2\frac{d\left(\sigma_\phi{}^2\right)}{dt}\bigg|_{RF}\right) \quad , \tag{17}$$

where $\Gamma_s = \left(\alpha_M - 1/\gamma^2\right)q\lambda_{RF}/\left(2\pi\nu_s\right)$ is the parameter of longitudinal focusing, λ_{RF} is the wave length of the RF voltage, ν_s it the longitudinal tune, α_M is the momentum compaction, q is the harmonic number and $\Delta P/P\big|_{sep}$ is the height of the RF bucket. There are two addends in Eqs. (16) and (17). The first addend is related to the momentum growth due to IBS and is determined by Eq. (11) in the parametric model described below. The second addend is related to the emittance growth due to RF noise with the growth rate for small amplitude equal to

$$\frac{d\left(\sigma_\phi{}^2\right)}{dt}\bigg|_{RF} = \pi\,\Omega_s{}^2\left(P_\phi\left(\Omega_s\right)+\frac{1}{2}\sigma_\phi{}^2 P_A\left(2\Omega_s\right)\right) \quad . \tag{18}$$

Here σ_ϕ is the bunch length in radians, Ω_s is the synchrotron frequency, and the spectral densities of the phase and amplitude noise are normalized as following

$$\overline{\delta\phi_{RF}{}^2} = \int_{-\infty}^{\infty} P_\phi(\omega)d\omega \quad , \quad \frac{\overline{\delta A_{RF}{}^2}}{A_{RF}{}^2} = \int_{-\infty}^{\infty} P_A(\omega)d\omega \quad . \tag{19}$$

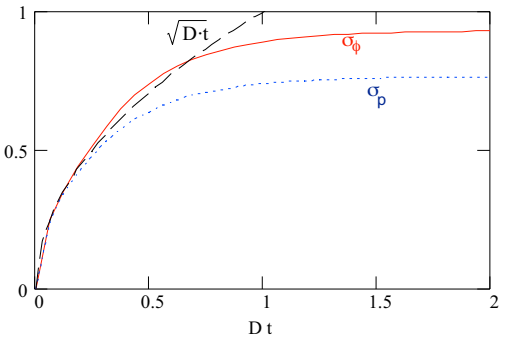

Figure 3. Dependence of rms bunch length (solid line) and momentum spread (dotted line) on time. Bunch length is expressed in radians. Momentum spread is expressed in $2p/p_{max}$ units, where p_{max} in the size of the bucket. Dashed line presents the dependence of bunch length and momentum spread on time for linear oscillator.

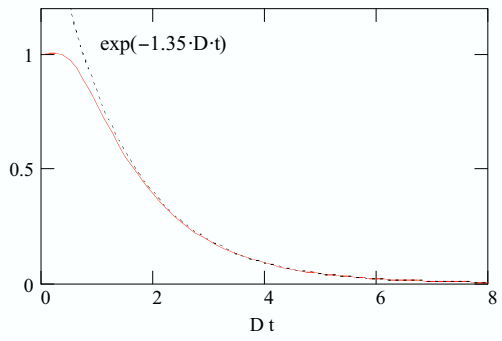

Figure 4. Dependence of relative bunch intensity (solid line) on time. Dotted line shows asymptotic exponential decay of the beam intensity.

The effect of the RF noise on the beam is dominated by the RF phase noise[3]. Presently its spectral density[5] is about $P_{\phi f}(\Omega_s/2\pi) = 4\pi P_\phi(\Omega_s) \approx 5\cdot 10^{-11}$ rad^2 / Hz, which causes the bunch lengthening of about 2200 mrad^2/hour. This value is more than an order of magnitude smaller than the longitudinal emittance growth due to IBS at the nominal proton intensity.

3.4. Parametric model

For gaussian beams the luminosity of the collider is determined by the well-known formula:

$$L = \frac{f_0 n_b N_p N_a}{2\pi\beta^* \sqrt{(\varepsilon_{px}+\varepsilon_{ax})(\varepsilon_{py}+\varepsilon_{ay})}} H\left(\frac{\sqrt{\sigma_{sp}{}^2 + \sigma_{sp}{}^2}}{\sqrt{2}\beta^*}\right) , \tag{20}$$

where n_b is the number of bunches, N_p and N_a are the number of protons and antiprotons per bunch, β^* is the beta-function in the interaction point (IP) and ε_{px}, ε_{py}, ε_{ax} are ε_{ay} are the horizontal and vertical emittances for proton and antiproton beams. The hourglass factor $H(x)$ takes into account the finite value of the longitudinal bunch size. It is equal to

$$H(x) = \frac{2}{\sqrt{\pi}} \int_0^\infty \frac{e^{-y^2}}{1+x^2y^2}\,dy \xrightarrow{x\le 3} \approx \frac{1}{\sqrt[3]{1+1.3x^2}} . \tag{21}$$

To describe the evolution of the luminosity we write a system of differential equations, which bounds up all basic parameters of the proton and antiproton beams:

$$\frac{d}{dt}\begin{bmatrix} \varepsilon_{px} \\ \varepsilon_{py} \\ \sigma_{pp}{}^2 \\ N_p \\ \varepsilon_{ax} \\ \varepsilon_{ay} \\ \sigma_{pa}{}^2 \\ N_a \end{bmatrix} = \begin{bmatrix} 2d\varepsilon_{px}/dt\big|_{BB} + d\varepsilon_{px}/dt\big|_{IBS} + d\varepsilon_{px}/dt\big|_{gas} \\ 2d\varepsilon_{py}/dt\big|_{BB} + d\varepsilon_{py}/dt\big|_{IBS} + d\varepsilon_{py}/dt\big|_{gas} \\ d\sigma_{pp}{}^2/dt\big|_{total} \\ -N_p\tau_{scat}{}^{-1} - dN_p/dt\big|_L - 2L\sigma_{p\bar{p}}/n_b \\ 2d\varepsilon_{ax}/dt\big|_{BB} + d\varepsilon_{ax}/dt\big|_{IBS} + d\varepsilon_{ax}/dt\big|_{gas} \\ 2d\varepsilon_{ay}/dt\big|_{BB} + d\varepsilon_{ay}/dt\big|_{IBS} + d\varepsilon_{ay}/dt\big|_{gas} \\ d\sigma_{pa}{}^2/dt\big|_{total} \\ -N_a\tau_{scat}{}^{-1} - dN_a/dt\big|_L - 2L\sigma_{p\bar{p}}/n_b \end{bmatrix} . \tag{22}$$

Here indices p and a denote protons and antiprotons, the derivatives $d\varepsilon/dt\big|_{BB}$ are the emittance growth rates due to scattering in the IP determined by Eq. (3) (factor of 2 takes into account 2 IPs), the derivatives $d\varepsilon/dt\big|_{IBS}$ are the emittance growth rates due to IBS determined by Eq. (11), the derivatives $d\varepsilon/dt\big|_{gas}$ are the emittance growth rates due to multiple scattering on the residual gas determined by Eq. (1), the derivatives $d\sigma^2/dt\big|_{total}$ are the momentum spread growth rates determined by Eq. (17), the derivatives $dN/dt\big|_L$ are the particle loss rate from bucket determined by Eq.(16), and the addends

[3] Main source of RF phase noise is a microphonics excited in a cavity due to flow of cooling water. RF phase feedback suppresses the noise by 30 db. That brings the noise to an acceptable level.

$2L\sigma_{p\bar{p}}/n_b$ determines particle loss in two collision points due to luminosity.

The model presented above was developed at the end of 2002 and resulted in a good agreement between the model predictions and the measurements for all parameters with exception of the particle loss from the RF bucket at the store beginning. This model overestimates it, because for any given bunch length the model implies some tails in the distribution function, and their presence leads to the particle loss. However, immediately after acceleration there is no tails because the bucket size at injection (~ 4 eV·s) is much smaller than the bucket size at 980 GeV (~10 eV·s). Additional complication is related to the fact that the initial longitudinal loss is not zero due to the single IBS scattering (Touschek effect), and there is a transition from the domination of loss by single scattering to the domination by multiple scattering. Taking into account that the IBS is the main diffusion mechanism for the proton beam we used an integro-differential equation, which simultaneously describes the single and multiple IBS scattering[6],

$$\frac{\partial f}{\partial t} = \int_0^\infty W(I,I')\left(f(I',t) - f(I,t)\right)dI' \quad . \tag{23}$$

Here the kernel is

$$\widetilde{W}(E,E') = \frac{D\omega_0\omega\omega'}{L_C(E-E')^2}\begin{cases} \dfrac{1}{2\omega} + \dfrac{I}{E'-E} & , \quad E' \geq E + \delta E \, , \\ \dfrac{1}{2\omega'} + \dfrac{I'}{E-E'} & , \quad E' \leq E - \delta E \, , \end{cases} \tag{24}$$

D is the diffusion coefficient, $L_C = \ln\left(\sqrt{I_{\max}/I_{\min}}\right)$ is the Coulomb logarithm, $I_{\min}$ and $I_{\max}$ are the minimum and maximum actions, ω_0 is the frequency of small amplitude motion, E and I are the energy and the action determined by Eq. (14), and $\omega = \partial E/\partial I$ is the action and the frequency. The divergence in Eq. (23) at $E \approx E'$ need to be confined for the energy difference below $\delta E \sim \omega_0 I_{min}$. Eq. (23) reduces to Eq. (13) if the large angle scattering is neglected.

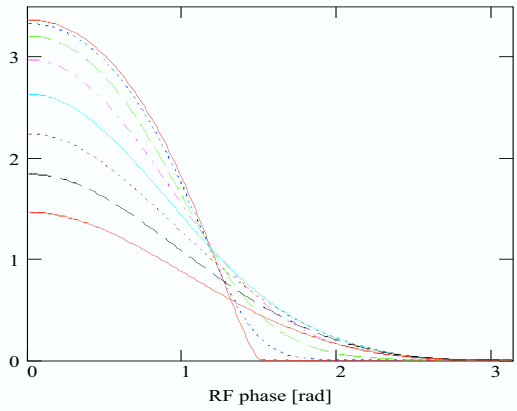

Figure 5. Numerical simulation of the longitudinal bunch profile evolution during the store in Tevatron.

Evolution of the longitudinal bunch profile in time obtained by numerical solution of Eq. (23) is presented in Figure 5. Unlike for the standard (local) diffusion the large non-gaussian tails are created from the very beginning. For a point-like beam the lifetime is determined by single scattering and is equal to $\tau_0 = 4L_C/D$. The lifetime decreases with beam expansion and, when the beam size achieves its maximum rms size of ≈0.931 rad, the lifetime reaches its asymptotic value of $\tau_0 \approx 0.741/D$. The parameterization of this numerical solution was done similar to Eqs. (15) – (17) and was used in the updated model which results are presented below.

Figure 6 presents measured and computed bunch parameters for the Store 2138 (Jan.05.2003). This store is comparatively well described by the model. The only free parameters used in the model were the residual gas pressure of $1.04 \cdot 10^{-9}$ Torr of molecular nitrogen equivalent, the coupling parameter $\kappa = 0.45$, and the spectral density of RF phase noise of $5 \cdot 10^{-11}$ rad^2/Hz.

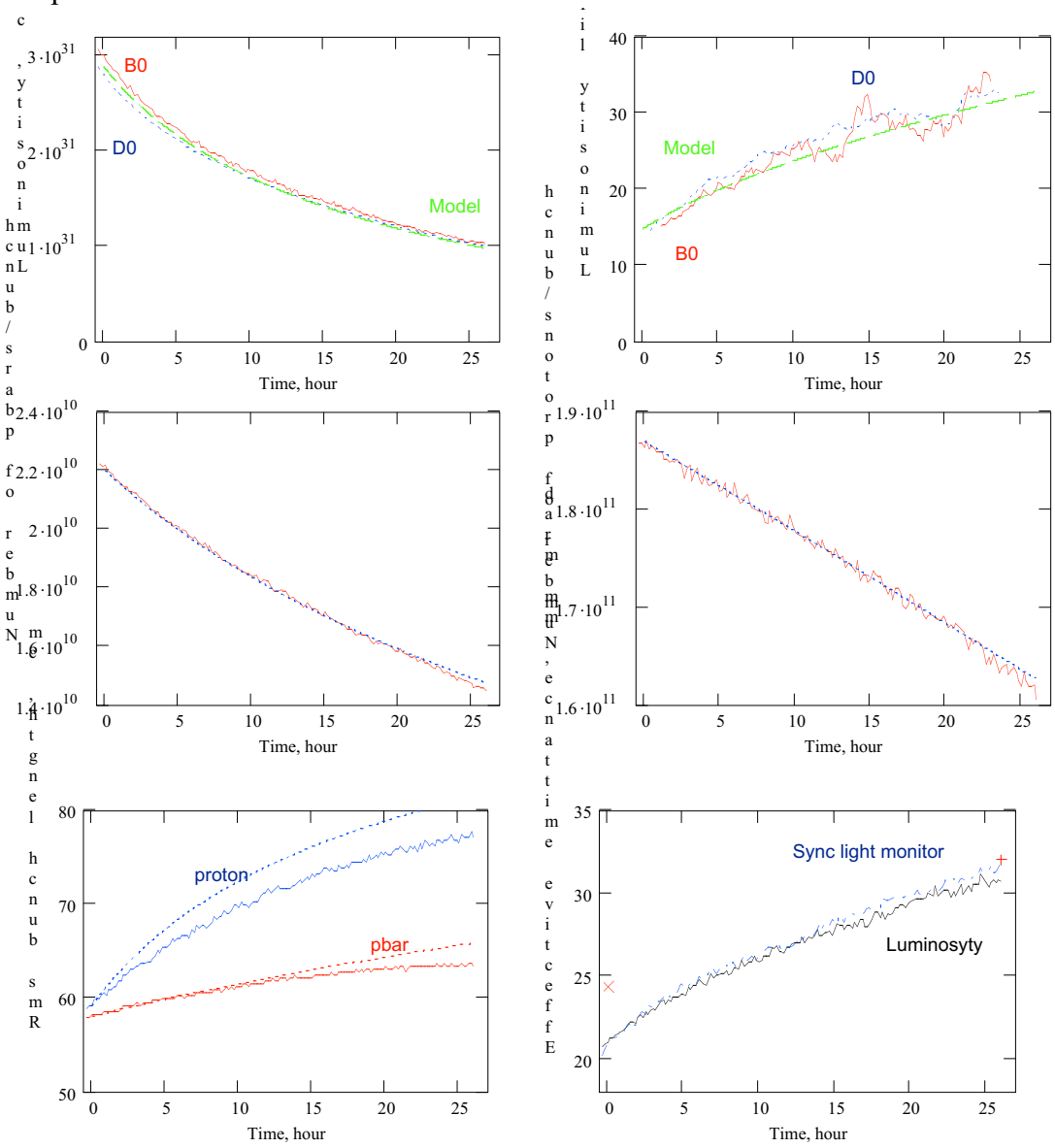

Figure 6. Dependencies of the luminosity and luminosity lifetime (top), antiproton and proton bunch intensities (middle), bunch lengths and effective emittance (bottom) on time for Store 2138. The top pictures present the CDF, D0 and model luminosities – solid, dotted and dashed lines correspondingly. The middle and left-bottom pictures present the measured (solid lines) and computed (dotted lines) intensities and longitudinal beam sizes. The right-bottom picture presents the beam effective emittances computed from the luminosity and from the emittances measured by the synchrotron light monitors. The crosses show the effective emittance build from emittances measured by the flying wires at the beginning and the end of the store.

As one can see the luminosity lifetime is predicted by the model with good accuracy. The computed proton and antiproton intensities are very close to the measured ones.

Measured and predicted particle losses are shown in Figure 7. Note that the measured particle loss is based on a single loss counter and is not "exactly" proportional to the total loss. Figure 8 shows computed particle loss due to different mechanisms. As one can see the longitudinal loss from the RF bucket is the major mechanism for proton loss. The loss due to luminosity is the major mechanism for antiproton loss.

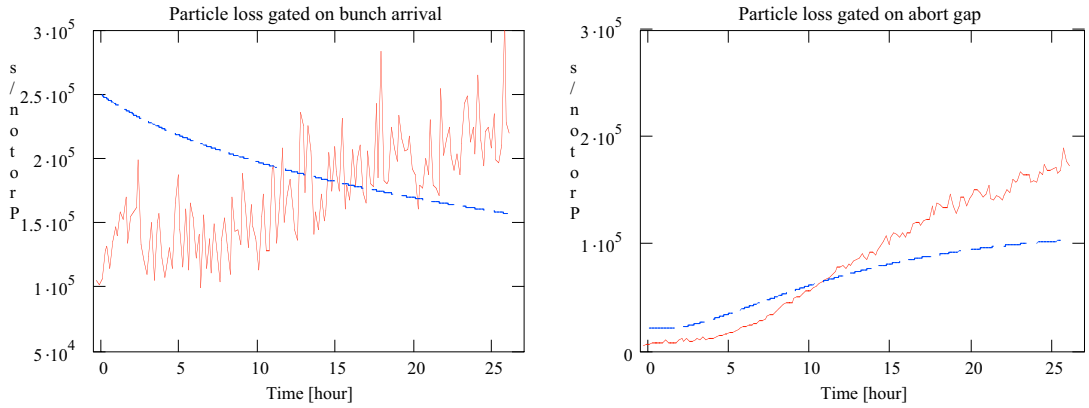

Figure 7. Dependence of computed (dashed lines) and measured particle loss (solid lines) per bunch on time for Store 2138.

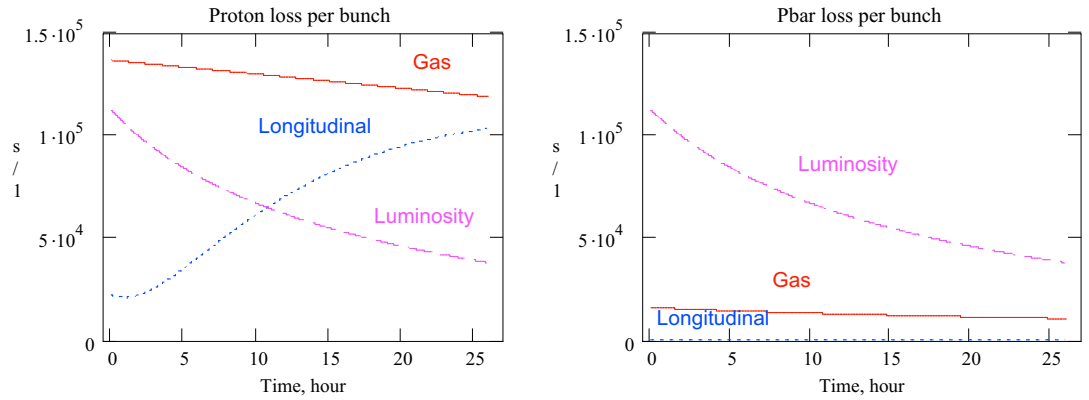

Figure 8. Dependence of particle loss on time computed from the model for different loss mechanisms for Store 2138.

The proton and antiproton lengthening (see Figure 6) is mainly driven by IBS and the model predicts about 20% faster growth than the measured one. The reason of this difference is still not understood.

Unfortunately there are no reliable emittance measurements and therefore some data massaging has been performed to compare the measurements and the model. The right-bottom picture in Figure 6 presents the beam effective emittances,

$$\varepsilon_{efff} = \sqrt{\left(\varepsilon_{px} + \varepsilon_{ax}\right)\left(\varepsilon_{py} + \varepsilon_{ay}\right)} \ , \qquad (25)$$

computed from the luminosity and from the emittances measured by the synchrotron light monitor. To match the curves the constant values were subtracted from the sync-light emittances. That takes out the contributions of light optics errors and diffraction. The relative scale of sync-light monitors was independently checked with local orbit bumps and found to be correct. It is also verified by coincidence of two curves in the right-bottom picture in Figure 6. Figure 9 presents comparison of the corrected sync-light

emittances, the emittances measured by flying wires at the beginning and at the end of the store and model emittances which initial values were adjusted to match the luminosity, bunch lengthening, and the flying wires emittance measurements at the end of the store. One can see that the antiproton vertical emittance grows significantly faster than the model prediction but because it is only one of four emittances contributing to the luminosity decay it does not produce any significant effect on the luminosity. Our present belief is that this fast vertical emittance growth is related to an amplification of the diffusion by the beam-beam effects (see next section).

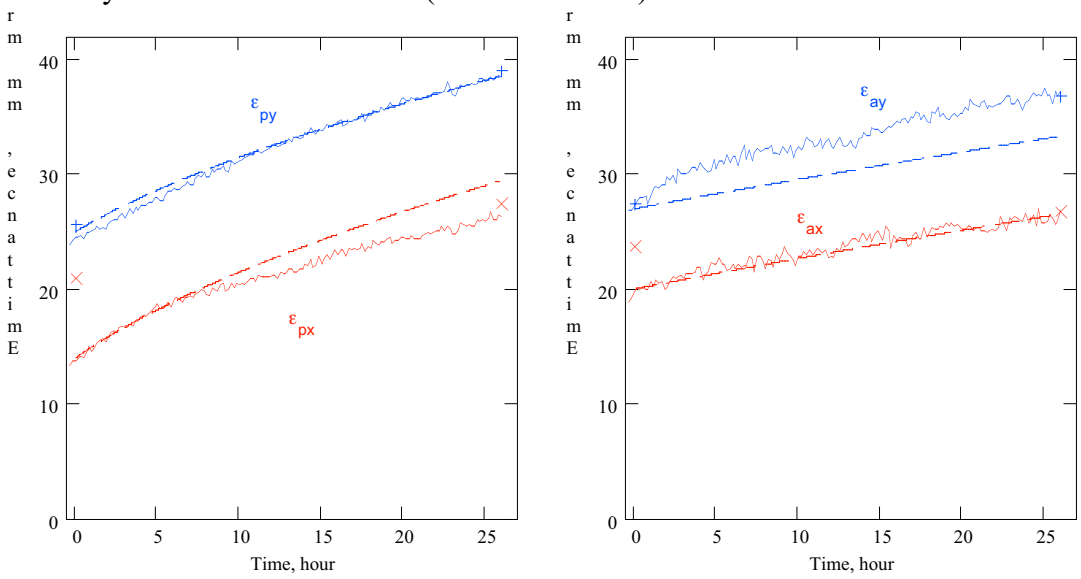

Figure 9. Dependence of proton (left) and antiproton (right) beam emittances on time for Store 2138; solid lines – the emittances measured by sync-light monitors; dashed lines – the computed emittances, crosses - the emittances measured by flying wires at the beginning and at the end of the store. The following values were subtracted from the sync-line emittances: $\Delta\varepsilon_{px}$=17 mm mrad, $\Delta\varepsilon_{py}$=5 mm mrad, $\Delta\varepsilon_{ax}$=21 mm mrad, $\Delta\varepsilon_{ay}$= 5 mm mrad.

The store 2138 discussed above has moderate discrepancies with the model and from this point of view can be considered as a normal store. The most of our stores are stronger influenced by the beam-beam interactions, but it still does not cause significant affect on the luminosity decay and the luminosity integral. Figure 10 presents measured and computed bunch parameters for the Store 2328 (Mar.20.2003). The same vacuum and RF noise spectral density were used in the model. Unlike Store 2138 the proton beam intensity decays faster than the model prediction, and the proton bunch length grows slower than the model prediction. Our present belief is that it is related to the beam-beam affect of antiprotons on the proton beam. The most probable reason is that small, uncontrolled changes of tunes combined with large proton bunch length affect the motion stability for particles with large synchrotron amplitudes. That causes both the particle loss and the bunch shortening (actually it was compensated by bunch lengthening due to IBS). Figure 11 demonstrates that this increase of particle loss is also well visible on the loss counters, which verify that the loss happens transversely. Figure 12 depicts computed linear tune shifts due to head-on beam-beam interactions in two IPs.

3.5. Luminosity scenario for final Run II parameters

As it follows from the results presented in the previous section the beam-beam interactions certainly affect the luminosity decay, but its effect is sufficiently small and the developed parametric model, with some reservations, can be used to analyze the luminosity dynamics for the final Run II parameters. An influence of beam-beam effects and instabilities on the beam parameters and the luminosity will be discussed later.

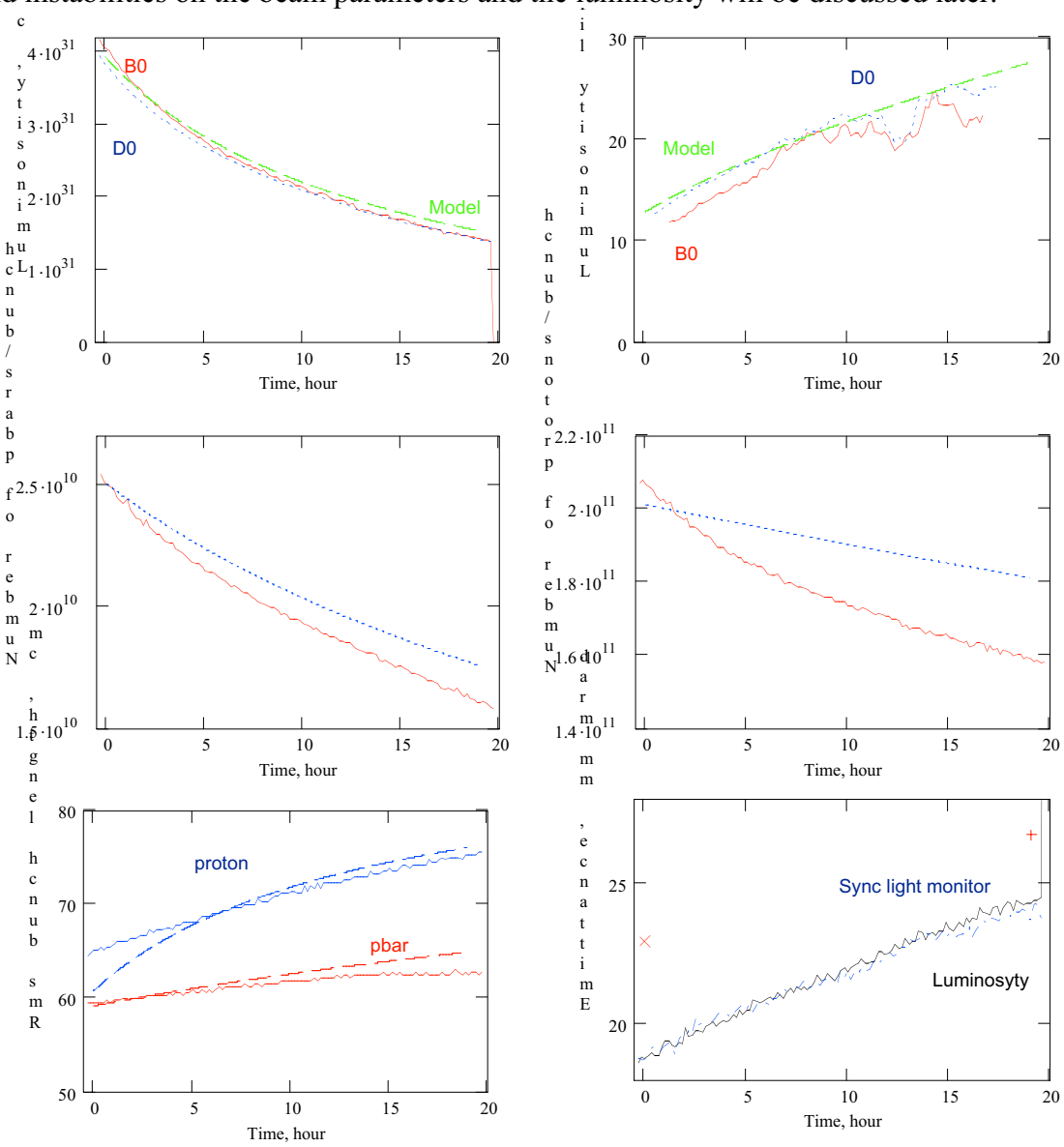

Figure 10. Dependencies of the luminosity and luminosity lifetime (top), antiproton and proton bunch intensities (middle), bunch lengths and effective emittance (bottom) on time for Store 2328. The top pictures present the CDF, D0 and model luminosities – solid, dotted and dashed lines correspondingly. The middle and left-bottom pictures present the measured (solid lines) and computed (dotted lines) intensities and longitudinal beam sizes. The right-bottom picture presents the beam effective emittances computed from the luminosity and from the emittances measured by the synchrotron light monitors. The following values were subtracted from the sync-line emittances: $\Delta\varepsilon_{px}$=17 mm mrad, $\Delta\varepsilon_{py}$=5 mm mrad, $\Delta\varepsilon_{ax}$=14 mm mrad, $\Delta\varepsilon_{ay}$= 2.5 mm mrad. The crosses show the effective emittance build from emittances measured by the flying wires at the beginning and the end of the store.

Table 3 presents parameters of the presently record Store 2328, typical collider parameters in April 2003 and projections for the final Run II parameters. Figure 13 depicts development of the collider parameters on time for the final Run II parameters. As one can see to achieve 7.2 times increase of the luminosity we plan to increase the number of antiprotons extracted from the stack by 4 times. The rest, 1.8 times, should come from the improvements in the antiproton transport and Tevatron. Three major contributors are an increase of the proton intensity by ~30%, an improvement of coalescing in MI, and improvements of antiproton transport (from the antiproton stack to the collisions in Tevatron). Two last items expected to yield an increase in the transfer efficiency from ~60% to 80%. The chosen proton intensity, $2.7 \cdot 10^{11}$ per bunch, corresponds to the linear head-on tune shift of 0.01 for each of two IPs. This is the maximum tune shift achieved in Run Ib with 6×6 bunch operation. We choose the maximum antiproton intensity to be half of the proton intensity. It is expected that further increase of antiproton intensity is limited by coherent beam-beam effects (strong-strong case) and by antiproton production.

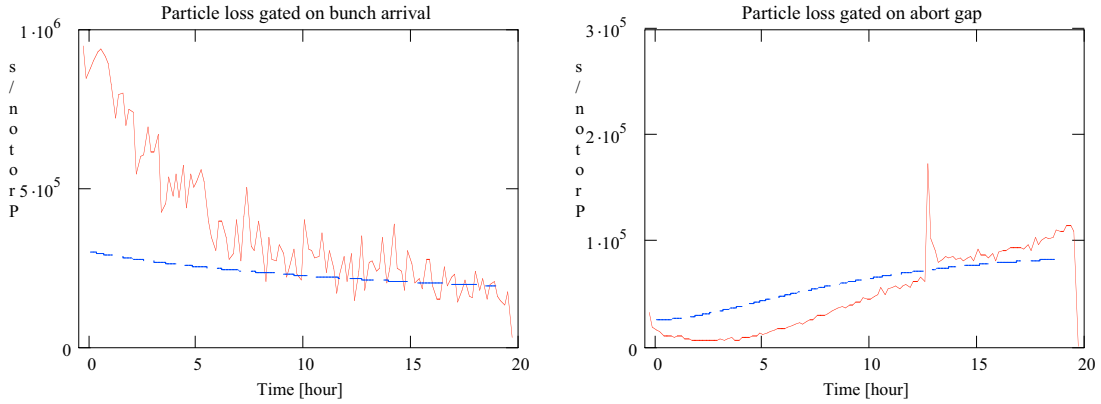

Figure 11. Dependence of computed (dashed lines) and measured particle loss per bunch on time for Store 2328.

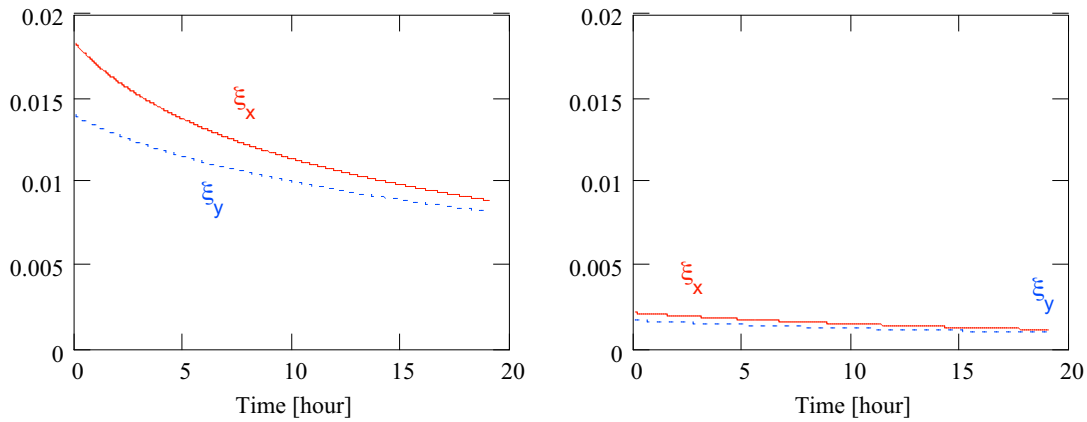

Figure 12. Dependence of computed beam-beam linear tune shifts for antiprotons (left) and protons (right) on time for Store 2328; solid lines – the horizontal tune shifts, dashed lines – the vertical tune shifts.

Top-left picture in Figure 13 presents the luminosity and the average luminosity computed as functions of time. The average luminosity is computed as the luminosity integral averaged over integration time and the shot setup time of 2 hour,

$L_{avg}(t) = \left(t + T_{setup}\right)^{-1} \int_{o}^{t} L(t')dt'$. In distinguish from the "instant" luminosity the average luminosity achieves its peak at approximately 7 hours and after this decreases comparatively slow. That implies that if we will lose in the antiproton production rate we can compensate most of this loss by lengthening of the store time. Figure 14 presents dependence of the average luminosity on the store duration time for different antiproton production rates.

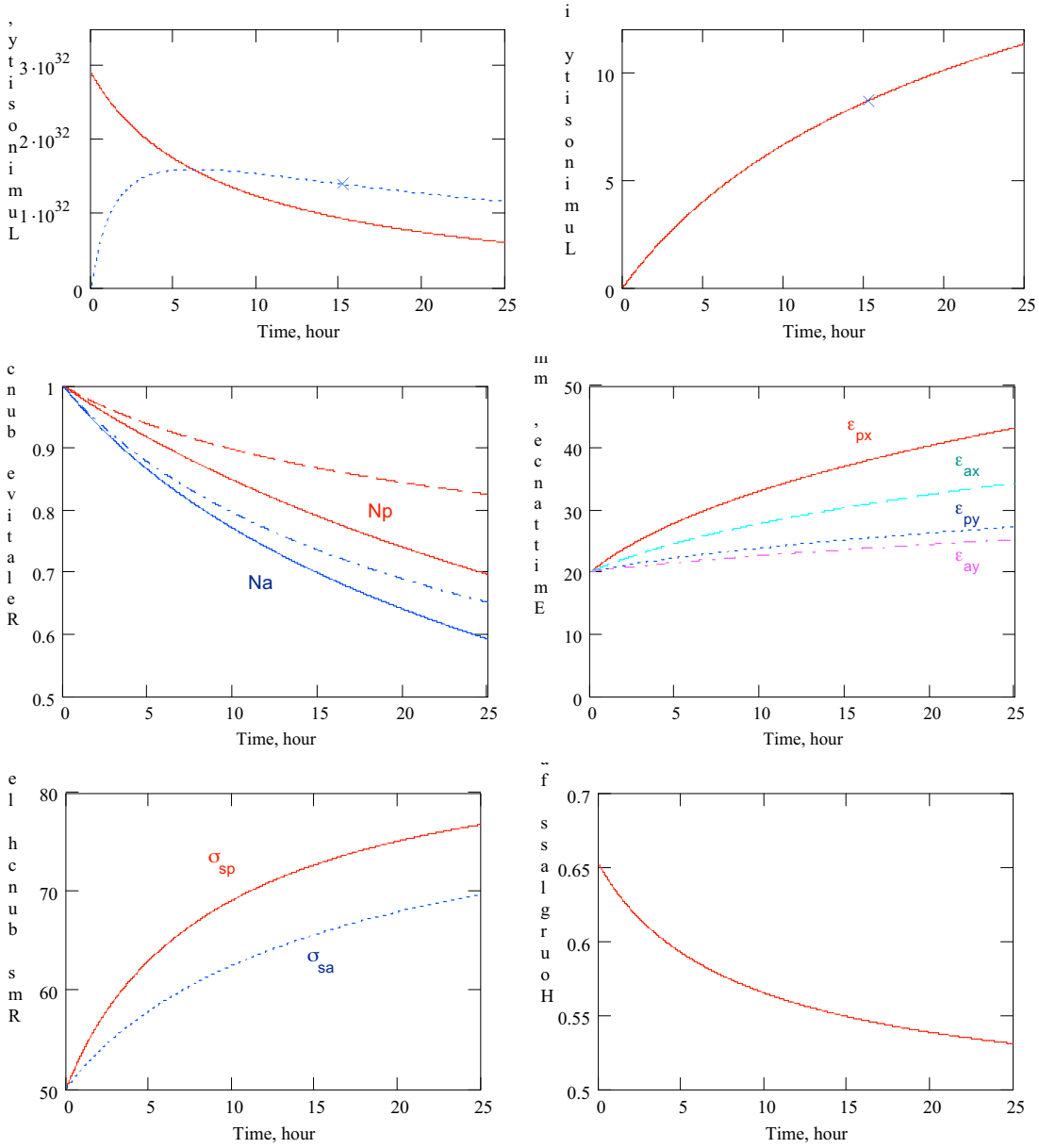

Figure 13. Dependencies on time for: *top-left* – the luminosity (solid line) and the average luminosity (dashed line); *top-right* – the luminosity integral; *middle-left* – the relative proton and antiproton intensities (solid lines) and intensity dropped due to scattering in IPs (dashed lines); *middle-right* – the beam emittances; *bottom-left* – the bunch lengths; and *bottom-right* – the hour glass factor, *H*. The crosses on the top pictures mark the store end.

Due to reduction of luminosity lifetime with growth of peak luminosity the averaged over store luminosity grows slower than the peak luminosity. The luminosity integral per year (in Table 3) is calculated presuming that the collider operates 46 weeks per year (6 weeks downtime or shutdown time); there is 48 hour downtime per week; and the shot setup time is not included into the downtime and is 2 hour.

Although IBS is the major source of beam heating there are many contributors to a finite luminosity lifetime. Table 4 presents the contributions of lifetimes for different beam parameters to the luminosity lifetime.

Table 3. Present and final Run II parameters of the collider

	Store 2328	Typical for April 2003	Final Run II
Number of protons per bunch, 10^{10}	20.7	20	27
Number of antiprotons per bunch, 10^{10}	2.54	2.2	13.5
Normalized 95% proton emittances, ε_x /ε_y, mm mrad	~14/24	~15/25	20/20
Normalized 95% antiproton emittances, ε_x /ε_y, mm mrad	~15/24	~16/25	20/20
Proton bunch length, cm	65	62	50
Antiproton bunch length, cm	59	58	50
Initial luminosity, 10^{30} $cm^{-2}s^{-1}$	40.5	35	290
Initial luminosity lifetime, hour	11	12	7.1
Store duration, hour	19	20	15.2
Luminosity integral per store, pbarn	1.71	1.2	8.65
Shot setup time, hour	2	2	2
Number of store hours per year	-	-	4800
Luminosity integral per year, fbarn	-	-	2.78
Transfer efficiency from stack to Tevatron at low-beta	60%	59%	80%
Average antiproton production rate, 10^{10}/hour	-	11	40
Total antiproton stack size, 10^{10}	166	150	610
Antiprotons extracted from the stack, 10^{10}	154	140	610

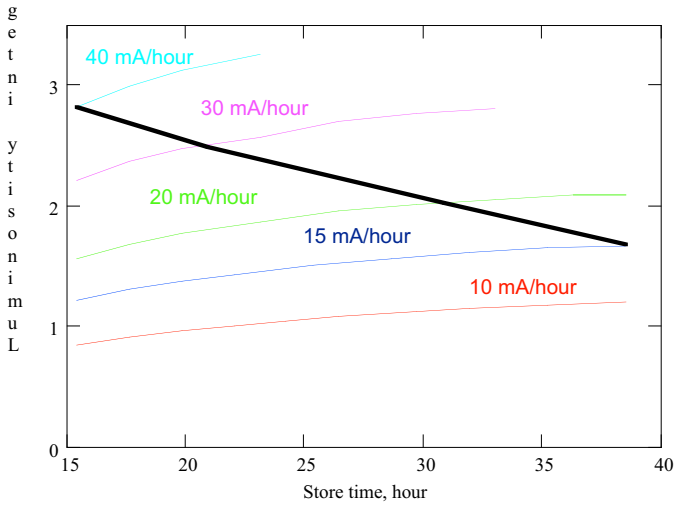

Figure 14. Dependencies of luminosity integral per year on the store time for different antiproton production rates. Thick solid line shows where intensity of antiproton beam reaches $1.35 \cdot 10^{11}$ per bunch.

Table 4. Break-up of the collider luminosity lifetime

	Lifetime [hour]
Luminosity	7.2
Prot.intens.	52
Pbar.intens.	29
Prot.H.emit.	9
Prot.V.emit.	32
Pbar.H.emit.	17
Pbar.V.emit.	56
Hourglass factor	32

References

1. V. Lebedev, S. Nagaitsev, Particle diffusion due to Coulomb scattering, EPAC 2002.
2. N.V.Mokhov, V.I.Balbekov, "Beam and luminosity lifetime", in *Handbook of Accelerator Physics and Engineering, 2-nd printing*, Ed. by A.W.Chao and M.Tigner, p.218, World Scientific (2002).
3. Lebedev V.A., et al., *NIM-A* **391**, 176-187 (1997).
4. J. D. Bjorken and S. K. Mtingwa, "Intrabeam scattering", *Particle accelerators*, (1983), v. 13, pp. 115-143.
5. J. Steimel, *et.al.*, "Effects of RF noise on the longitudinal emit. growth in Tevatron," Proceedings PAC2003.
6. Burov, private communication, 2003.